Stability and Bifurcation Analysis of Multi-Element Non-Foster Networks

Almudena Suárez, *Fellow, IEEE*, Franco Ramírez, *Senior Member, IEEE*

***Abstract*— A stability and bifurcation analysis of multi-element non-Foster networks is presented, illustrated through its application to non-Foster transmission lines. These are obtained by periodically loading a passive transmission line with negative capacitors, implemented with negative-impedance converters (NIC). The methodology takes advantage of the possibility to perform a stability analysis per subintervals of the perturbation frequency. This will allow an independent analytical study of the low-frequency instability, from which simple mathematical criteria will be derived to prevent bias-network instabilities at the design stage. Then, a general numerical method, based on a combination of the Nyquist criterion with a pole-zero identification of the individual NIC, will be presented, which will enable the detection of both low and high frequency instabilities. A bifurcation analysis of the multi-element non-Foster structure will also be carried out, deriving the bifurcation condition from a matrix-form formulation of the multi-element structure. The judicious choice of the observation ports will enable a direct calculation of all the coexisting bifurcation loci, with no need for continuation procedures. These bifurcation loci will provide useful insight into the global-stability properties of the whole NIC-loaded structure.**

***Index Terms*—Non-Foster network, stability, bifurcation, Non-Foster transmission line**

I. Introduction

Non-Foster circuits [1]-[6] are based on the use of negative capacitors or inductors, implemented through transistor-based negative impedance converters (NICs) [1]-[3], [7]-[8]. The non-Foster circuits have been applied for broadband impedance matching of electrically small antennas [1]-[2], [5], [9]-[10] and other system components. They also enable the realization of fast-wave transmission lines [6], [11]-[13], which allow the control of the phase delay of guided-wave devices, applied on squint-free beamforming of antenna arrays [13]-[16]. Other interesting metamaterial realizations can be found in [17]-[20]. The fast-wave propagation is achieved by periodically loading [6], [11]-[14] the transmission line with negative capacitors, implemented with transistor-based configurations. However, a problem inherent to circuits based on non-Foster elements is the likelihood of unstable behavior, since any NIC is a potentially unstable two-port network [1]-[6]. Using the NIC *h*-parameter matrix [3], it is shown that any practical two-port NIC is always short-circuit stable (SCS) and open-circuit unstable (OCU) at one port (that is, when terminating that port in a short-circuit and an open circuit, respectively), and open-circuit stable (OCS) and short-circuit unstable (SCU) at the other port. In fact, the great potentiality of non-Foster circuits may be severely limited by their unstable behavior.

Several previous works have addressed the stability analysis of non-Foster circuits [3]-[5], [17], [21]-[24]. Some of them rely on simplified equivalent networks of the loaded NIC [2], represented as a negative capacitor (or inductor), which is unrealistic. When considering the transistor-based NIC, most of the stability analyses presented are based on time-domain integration, applying a Gaussian pulse [5], or on the Nyquist criterion [4], [22]. The time-domain analysis may be unreliable since transients can be very long in NIC circuits, as demonstrated in [25]. On the other hand, when using the Nyquist criterion care must be taken in the selection of the complex function to which the Nyquist criterion is applied. This function should not contain any poles of the right-hand side of the complex plane (RHS) [26]-[29]. This is because the number N_{cir} of clockwise encirclements of the Nyquist plot around the origin provides the difference between the number N_Z of RHS function zeroes (agreeing with the number of RHS *system* poles) and the number N_P of RHS function poles, that is, $N_{cir} = N_Z - N_P$ [26]. Thus, unless $N_P = 0$, the result will be inconclusive. The condition $N_P = 0$ is ensured through the use of the Normalized Determinant Function (NDF) [28]-[29]. The NDF is calculated at the intrinsic device terminals. In this way all the possible feedback effects, including those resulting from parasitic elements inside the device models [30], are taken into account. If the analysis is not performed at the intrinsic terminals, the determinant may exhibit RHS poles, resulting from the interaction of the passive and purely active elements. In the case of black-box models, circuit-simulator models may be used. However, this may be problematic if the original black box includes multiple reactive effects, since the analysis must be performed in a large frequency interval, only limited by the device filtering effects.

In this work we propose the use of pole-zero identification [31]-[33] to ensure the stable behavior of the active components

Manuscript received July 1, 2017. This paper is an expanded version from the 2017 International Microwave Conference, Honolulu, HI, 4–9 June 2017. This work was supported by the Spanish Ministry of Economy and Competitiveness and the European Regional Development Fund (ERDF/FEDER) under research projects TEC2014-60283-C3-1-R and TEC2017-88242-C3-1-R.

A. Suárez and F. Ramírez are with Dpto. Ingeniería de Comunicaciones, Universidad de Cantabria., Av. Los Castros 39005, Santander, Spain (e-mail: suareza@unican.es; ramirezf@unican.es).

or blocks. This method relies on the fact that all the transfer functions [31]-[33] defined in a same linear system share the same denominator. It is based on the fitting of a transfer function with a quotient of polynomials, which provides the zeroes and poles with good accuracy. Thus, it is not necessary to calculate the transfer functions at the intrinsic device terminals, so, the method is fully compatible with the use of black-box models for the active devices. Nevertheless, exact pole-zero cancellations may occur in a particular transfer function, so two or more functions must be generally tested. Pole-zero identification [31]-[33] has recently been applied to non-Foster circuits [22], presenting pole-zero maps for particular circuit-component values, without a detailed investigation of the causes for the instability phenomena.

The recent work [25] presents an in-depth stability analysis of a typical non-Foster matching network, applicable for antenna matching. Using analytical derivations as well as pole-zero identification, two different instability mechanisms are detected. The first one is associated with the presence of real poles of low magnitude, caused by feedback effects inherent to the NIC transistor configuration. The second one is associated with poles of higher magnitude, detectable in a higher frequency interval. This instability was found to be due to the dominance of the negated impedance over the circuit passive-loading effects, in a manner similar to what is described in [21], [34]. However, the analytical formulations and numerical methodologies presented in [25] were restricted to a non-Foster circuit based on a single NIC. The aim of this work is to extend the investigation to networks containing multiple NICs, as in the case of fast-wave transmission lines [6], [11]-[15], which are periodically loaded with NIC elements.

Several procedures will be presented with two different objectives: getting insight into the instability mechanisms and providing useful methodologies to predict and suppress instability at the design stage. The procedures take advantage of the possibility to perform the stability analysis per subintervals of the perturbation frequency, as is usually done in the numerical pole-zero identification [31]-[33]. This will allow distinguishing the mechanism for low frequency instabilities from other instabilities detectable at higher frequencies. In fact, the transistor cross-coupled configuration is prone to give rise to unstable real poles [25], which can be predicted with an analytical formulation. The formulation will enable a convenient derivation of stability criteria, in terms of the transistor transconductances, biasing elements and number of cells, of easy evaluation at the design stage. The bifurcation phenomenon [35]-[41] that gives rise to the circuit instability will also be determined, deriving the bifurcation condition that defines the low-frequency stability boundary.

Regarding the high frequency instabilities, the insightful work [42] is based on the derivation of analytical expressions to describe the frequency response of the non-Foster transmission line. However, ideal negative elements are considered instead of transistor-based NICs. Here the stability analysis will be carried out in a numerical manner, using complete and realistic models of all the elements in the NIC-loaded line. This is preferred due to the complexity of the transistor-device models and the impact of parasitics. The method will be based on a combination of pole-zero identification [31]-[33] and the Nyquist criterion [26].

The bifurcation phenomenon [35]-[37] that gives rise to the higher-frequency instabilities will also be identified and the bifurcation condition will be derived from a matrix-form formulation of the multi-element structure. The judicious choice of the observation ports will enable a direct calculation of all the coexisting bifurcation loci, with no need for continuation procedures. Note that the goal of this work is not the investigation on the fast-wave transmission line, which has been done by other authors [6], [11]-[14], but on their stability and bifurcation behavior, as well as the derivation of accurate and easy-to-use stability-analysis methodologies.

The paper is organized as follows. Section II summarizes the methodology to obtain a non-Foster transmission line, based on the topology proposed in [11]-[12]. Section III presents the analytical formulation to predict instabilities associated with the bias network, as well as design criteria. Section IV presents the general numerical methodology for stability analysis. Section V describes a practical technique to obtain the instability boundary.

II. Non-Foster Transmission Line

Following the methodology in [6], [11]-[14], the non-Foster transmission line is implemented through the periodic loading of this line with negative capacitors. Neglecting resistive contributions, the phase constant of the original passive transmission line is given by:

$$\beta_p = \omega\sqrt{l_x\ c_x} = \frac{\omega}{c}\sqrt{\varepsilon_{eff}} \tag{1}$$

where l_x and c_x and the inductance and capacitance per unit length, respectively, c is the speed of light and ε_{eff} is the effective dielectric constant. The phase constant can be decreased by reducing the effective line capacitance through the periodical connection of negative capacitors. Assuming the parallel connection of one capacitor per length Δx, the phase constant becomes [15]:

$$\beta_{nF}(\omega) = \omega\sqrt{l_x\left(c_x - \frac{C_{neg}}{\Delta x}\right)} \tag{2}$$

where C_{neg} has been defined as a positive quantity. Note that the radicand is frequency dependent, since the negative capacitance can only be achieved in a certain frequency band. In order to avoid backward propagation, the total capacitance must be positive [7]-[8], so the following condition must be fulfilled:

$$c_x - \frac{C_{neg}}{\Delta x} > 0 \tag{3}$$

In a practical realization, the Non-Foster transmission line will contain a limited number N of Δx cells, corresponding to a total length L. To achieve fast wave propagation in a certain bandwidth, the phase delay through the line of length L must be smaller than the one resulting from light passing through the vacuum [6], [11]-[14].

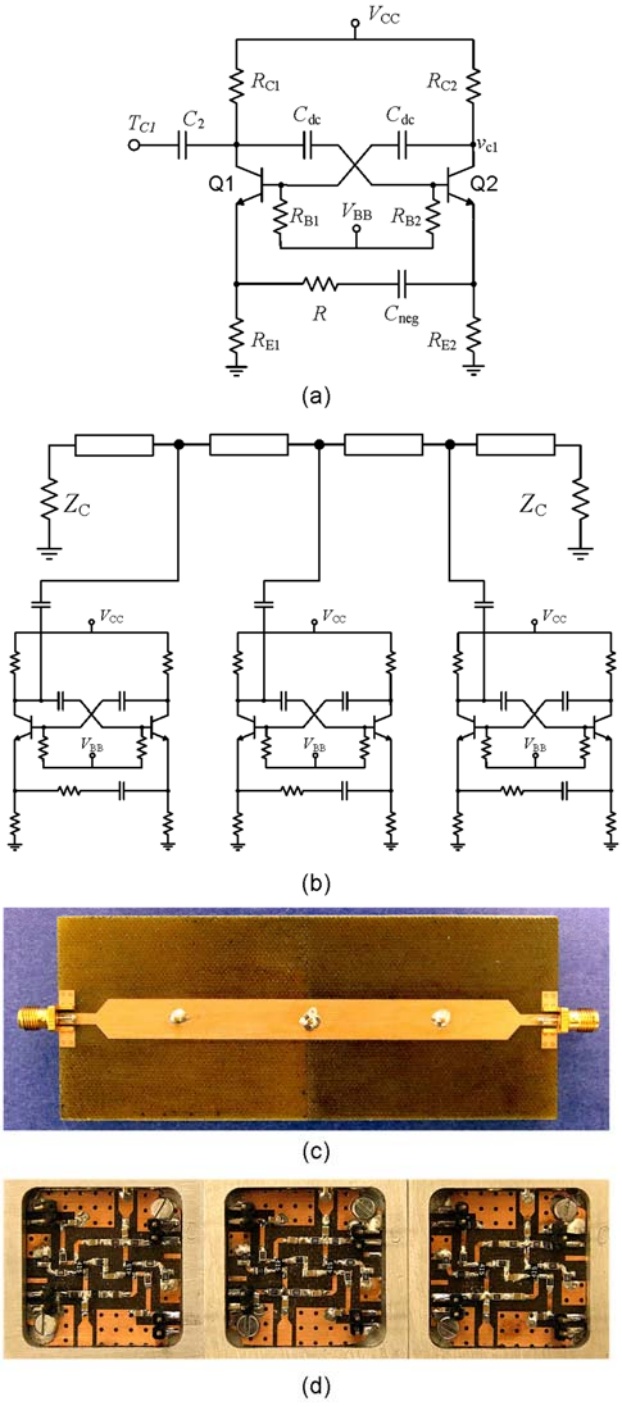

Fig. 1 Schematic of the fast-wave propagation transmission line, adapted from [7]-[8]. (a) NIC circuit, loaded with C_{neg} and R. The resistance R may be used only in an auxiliary manner, for analysis purposes. The connection nodes to the transmission line correspond to the collector of the first transistor T_{C1} and ground. (b) Transmission line periodically loaded with the NICs.(c) and (d) Photographs of the top and bottom views of the fabricated prototype [FR-4 (ε_r = 4.4, h = 1.6 mm) substrate, using AVAGO AT41511 transistors].

The negative capacitance is obtained by using NICs, terminated a positive capacitor. The NIC chosen here is based on bipolar transistors, with the topology proposed in [11]-[12]. It uses two cross-coupled transistors, with a capacitor C_{neg}, connected between their emitter terminals [Fig. 1(a)]. According to [11]-[12], this topology, which also includes base, collector and emitter resistors, reduces the impact of discrepancies between the transistor elements. The NIC is connected to the transmission line through the collector terminal T_{C1}. As previously reported [1], when the NIC input port is defined at the collector terminals, it is short-circuit stable, or stable when terminating the port in an impedance smaller than the input one. As argued in [11]-[12], this should be the case when introducing the NIC terminated in the capacitor C_{neg} into the transmission line, due to the condition (3). However, these stability considerations, in terms of open and short-circuit terminations, derive from a number of simplifying assumptions, with the two-port network described with a constant *h*-parameter matrix [3]. Therefore, a rigorous stability analysis at circuit level is essential.

Since, as stated, the aim of this work is not the fast-wave transmission line design but the investigation of its stability properties, the test-bench is very similar to the one presented in [11]-[12]. The transmission line is implemented on the substrate FR-4 (ε_r = 4.4, h = 1.6 mm). In a similar way as [11]-[12], N = 3 transmission-line sections are considered [Fig. 1(b)], though extensions to an arbitrary number N will also be assumed at some instances. As in [11]-[12], the length and width of the distributed transmission line sections are 33.3 mm and 10 mm, respectively. The negative capacitors $-C_{neg}$ are implemented through the NIC shown in Fig. 1(a). Biasing inductors have been avoided since, as verified with the formulation presented in Section III, they make the circuit stable behavior even more critical, in agreement with previous reports [2], [9]-[10]. Accurate models of all the active elements, provided by Modelithics, will be used in all the simulations, though in Section II simplified analytical models will also be considered for an insightful investigation of the low-frequency instability.

The biasing circuitry consists of the dc blocking capacitor C_2, in series with the collector terminal T_{C1}, and C_{dc}, in the cross-coupling branches, and the resistors R_{Bi}, R_{Ci} and R_{Ei}, where i = 1,2. Note that different values of these resistors are used, in principle, for the two transistors, since the NIC (with its input port defined between the collector terminal T_{C1} and ground) is not symmetric. An additional resistor R, connected in series with the capacitor C_{neg}, is also considered, as in some previous works [3]. The resistor R may not be necessary, but will facilitate the calculation of the instability boundaries in Section IV, even if the actual design has R = 0 Ω.

After a preliminary design of the NIC circuit, the whole non-Foster transmission line has been optimized in order to achieve a superluminal phase delay in the frequency band comprised between 1 MHz and 200 MHz. This has been done by considering M evenly-spaced frequency points, $f_m = f_o + m\Delta f$, where m = 0 to M–1. The objective is to get a non-dispersive phase delay, fulfilling $\Delta\phi = -\tau\omega$, where τ is the time delay, which must satisfy $\tau < L/c$, under the constraint of a total positive capacitance [as in (3)]. The optimization is carried out through M single-point scattering-parameter simulations of the same 3-cell transmission line (with common element values), at the frequencies f_m, where m = 0 to M–1. The M goals are $\Delta\phi_m = -\tau 2\pi f_m$. The value of the delay τ is progressively

reduced, in a sequence of *M*-goal optimizations. The optimized elements are the capacitor C_{neg}, the resistor R and the biasing resistors. The results for the values V_{CC} = 9 V, R_{C1} = 300 Ω, R_{C2} = 47 Ω, R_{E1} = 100 Ω, R_{E2} = 257 Ω, C_{neg} = 10 pF and R= 0 Ω are shown in Fig. 2(a).

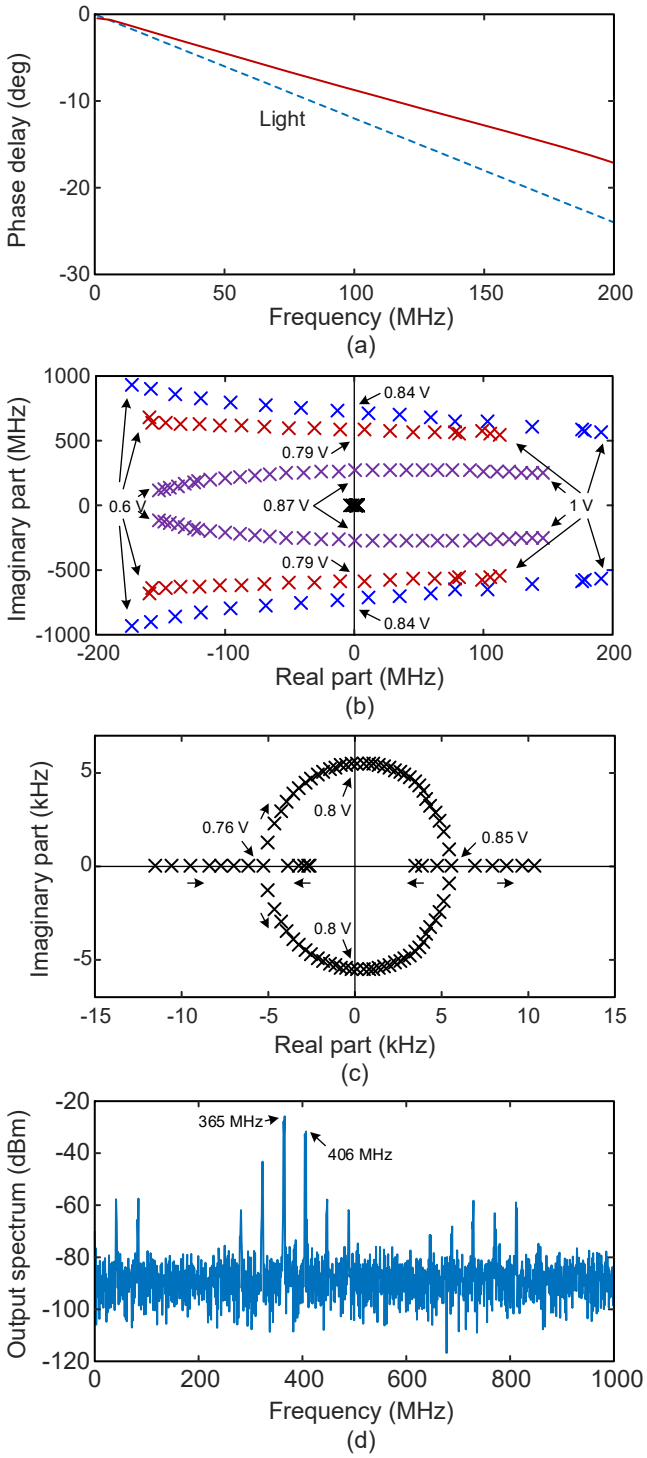

Fig. 2 Optimization of the fast-wave transmission line. (a) Variation of the phase delay versus the input frequency obtained through multiple single point optimizations. (b) Stability analysis through pole-zero identification. The real part of the dominant poles has been represented versus V_{BB}. There are three pairs of critical complex-conjugate poles and two critical real poles.(c) Expanded view of the pole locus in the low-frequency range. (d) Measured mixer-like spectrum, with two fundamental frequencies.

The stability analysis of the resulting circuit has been carried out through pole-zero identification [31]-[33]. As stated in the introduction, this method is based on the fact that all the transfer functions that can be defined in a linear system share a same denominator, which formally agrees with the system characteristic determinant. For the stability analysis, the circuit is terminated with 50 Ohm impedances, although any other arbitrary termination may equally be considered. In most cases, the transfer-function used is of impedance type, though an admittance type transfer function [33] can also be considered and will be used later in this work. In the impedance-type case, a small-signal current generator at the frequency f is introduced at a sensitive circuit node, such as those corresponding to the active devices. The transfer function $Z(f)$ is defined as the ratio between the node voltage and the current introduced. The poles, which are common to all the possible transfer functions, are obtained by applying pole-zero identification to $Z(f)$. The procedure in the case of an admittance-type transfer function [31-33] would be analogous.

Pole-zero identification has been applied under variations of the bias voltage V_{BB}. In Fig. 2(b), the variation of the imaginary and real part of the poles has been represented versus V_{BB}. There are three pairs of critical complex-conjugate poles and two critical real poles, which cross the imaginary axis at different V_{BB} values. In fact, the detection of the unstable real poles is demanding and requires an identification in the extremely low frequency interval 100 Hz≤ f ≤100 kHz . Fig. 2(c) presents an expanded view of the pole locus in the low-frequency range, showing how the two real poles merge into a pair of complex-conjugate poles just before crossing the imaginary axis. Then, they split again into two real poles, one of which approaches the exis but never crosses to the LHS. The presence of both real and high frequency poles indicates a complex unstable behavior, which will be difficult to predict and control through a standard application of the available methodologies. The design was measured at V_{BB} = 0.85 V and found to be unstable [Fig. 2(d)], in agreement with the predictions of Fig. 2(b). The measured spectrum is shown in Fig. 2(c). It is a mixer-like spectrum, with two fundamental frequencies. The incommensurate spectral lines with the highest power are at 364 MHz and 406 MHz. For V_{BB} = 0.85 V, the poles at about 320 MHz in the simulation of Fig. 2(b) have not crossed the imaginary axis yet, since the Hopf bifurcation occurs at V_{BB} = 0.87 V. However, small discrepancies in the component models would justify the observation of the corresponding oscillation at the lower bias voltage V_{BB} = 0.85 V. As stated, the second most significant incommensurate frequency in the measured spectrum is slightly above 400 MHz. This should correspond to the one above 500 MHz in the pole analysis. Although the two frequencies do not agree, inspection of Fig. 2(b) shows the high sensitivity of the frequency of this second pair of critical poles to V_{BB}. In addition, one should take into account that, in general, poles only predict the oscillation frequency at the initial start-up transient, when the oscillator still behaves in a linear manner. As the oscillation amplitude continues to grow, there can be a significant variation of the oscillation frequency, due to nonlinear effects. This will be more remarkable under low a quality factor, as is the case of this circuit, mostly composed of capacitive and resistive elements. The frequency corresponding

to the third pair of critical poles does not appear in the spectrum as an independent fundamental. This is because the quasi-periodic solution measured has stabilized through inverse bifurcations [35]-[41], at which the additional critical poles have crossed to the left-hand side of the complex plane (LHS).

As stated, the low-amplitude real poles and the complex-conjugate poles are obtained through identification in a low frequency band and a higher frequency band, respectively. This property will enable the distinction of the mechanism giving rise to the low-amplitude real poles from other instabilities, detectable at higher frequencies, including those associated with the impedance negation. In the following section, a detailed analytical study of the low-frequency instability is presented.

III. Low-Frequency Instability

Initially, the instability due to real poles on the RHS will be studied. This should be detectable by considering a small perturbation frequency, so most of the transistor parasitic elements can be neglected, as well as the pair *R*-C_{neg}, behaving basically as an open circuit, which is due to the high value of the impedance associated with C_{neg} in the low-frequency range. On the other hand, the transmission line sections can be considered as short circuits. Under these simplifications, in the case of an *N*-cell transmission line, the low-frequency equivalent circuit approximately consists of the parallel connection of *N* one-port blocks with the input admittance Y_{in} and two termination impedances, as shown in the schematic of Fig. 3(a). Results will be validated through comparison with complete circuit-level simulations using models from Modelithics and with measurements.

For the stability analysis of the circuit in Fig. 3(a), a small perturbation of complex frequency *s* is considered. Applying Kirchoff's laws to the equivalent circuit in Fig. 3(a), one obtains the following characteristic equation:

$$\frac{2}{Z_o}+N\ Y_{in}(s)=\frac{2}{Z_o}+N\frac{num(s)}{den(s)}=0 \tag{4}$$

where *num*(s) and *den*(s) are the numerator and denominator of $Y_{in}(s)$. In (4) the line has been assumed to be terminated in Z_o = 50 Ω. However, the analysis can be easily extended to arbitrary termination impedances. Provided that there are no cancellations of RHS zeroes and RHS poles in the function $Y_{in}(s)$ (which should be checked in a separate manner), the stability properties of the whole configuration in Fig. 3(a) will be determined by the roots of the following characteristic polynomial:

$$2G\ den(s)+N\ num(s)=0 \tag{5}$$

where $G=1/Z_o$. All the roots of (5), agreeing with the system poles, should have a negative real part. The characteristic equation (5) is of general application regardless of the particular bias network, defining the form of $Y_{in}(s)$. In fact, the bias network considered in Fig. 1 is just a particular case, considered for illustration.

The NIC input admittance at low frequencies, Y_{in}(s), will be calculated using simplified low-frequency models of the transistor devices, in which all the capacitive and inductive elements can be neglected. Resistive elements might be needed in some cases, but here a very good prediction of the stability properties has been achieved without these elements, so they will also be neglected for a better insight. Thus, the transistors are modeled with ideal linear transconductance functions $g_{mi}V_i$, where i =1,2. For each bias point (of each transistor device), the g_m in the simplified model of the bipolar transistor is estimated as $g_m = I_c/25.9$ mS [43]. This provides the simplified equivalent circuit of Fig. 3(b). Note that this is just an example of equivalent low-frequency circuit, since the method can be extended to other bias-network topologies.

To calculate the low-frequency Y_{in}(s), the equivalent circuit in Fig. 3(b) is excited with the AC voltage source V_{in}. Applying Kirchoff's laws, one obtains the following linear system:

$$\begin{aligned}
&-\left(p+\frac{1}{C_{dc}s}q\right)I_2+V_{in}=\frac{1}{C_2 s}I_{in}\\
&I_1+\left(a_1+\frac{1}{C_{dc}s}b_1\right)I_2=I_{in}\\
&\left(a_2+\frac{1}{C_{dc}s}b_2\right)I_1+I_2=0
\end{aligned} \tag{6}$$

where I_{in} is the current through the voltage source and the following parameters have been defined:

$$\begin{aligned}
p&=R_{E2}+1/g_{m2}\\
q&=(R_{E2}+1/g_{m2})G_{B2}\\
a_1&=(R_{E2}+1/g_{m2})(G_{B2}+G_{C1})\\
a_2&=(R_{E1}+1/g_{m1})(G_{B1}+G_{C2})\\
b_1&=(R_{E2}+1/g_{m2})G_{B2}G_{C1}\\
b_2&=(R_{E1}+1/g_{m1})G_{B1}G_{C2}
\end{aligned} \tag{7}$$

Note that the conductances $G_B = R_B^{-1}$, $G_C = R_C^{-1}$, $G_E = R_E^{-1}$ have been defined. The input admittance Y_{in} is obtained as the ratio $Y_{in} = I_{in}/V_{in}$. It is easily seen that the resulting expression has no inherent cancellations of zeroes and poles. Replacing the expression for $Y_{in}(s)$ into (5), one obtains the following third-order characteristic polynomial:

$$\alpha_3 s^3+\alpha_2 s^2+\alpha_1 s+\alpha_0=0 \tag{8}$$

where all the coefficients are constant quantities, given by:

$$\begin{aligned}
\alpha_3&=C_2 C_{dc}^{\ 2}(Ga_2 p+Na_1 a_2-N)\\
\alpha_2&=C_{dc}\begin{pmatrix}C_2 G(a_2 q+b_2 p)+NC_2(a_1 b_2+a_2 b_1)\\+C_{dc}G(a_1 a_2-1)\end{pmatrix}\\
\alpha_1&=C_2 G b_2 q+NC_2 b_1 b_2+C_{dc}G(a_1 b_2+a_2 b_1)\\
\alpha_0&=Gb_1 b_2
\end{aligned} \tag{9}$$

In view of the positive sign of α_0, a necessary condition for stability is $\alpha_1,\alpha_2,\alpha_3>0$. From the inspection of (9), the coefficients α_1,α_2 can be either positive or negative. A critical quantity is $a_1 a_2-1$, which may become negative for high transistor gain and different combinations of (low) emitter resistors and (high) collector resistors. However, even if the

condition on the equal sign of the polynomial coefficients is fulfilled, the system may be unstable since the Routh-Hurtwiz criterion [26] involves the evaluation of other parameters, depending on the polynomial coefficients.

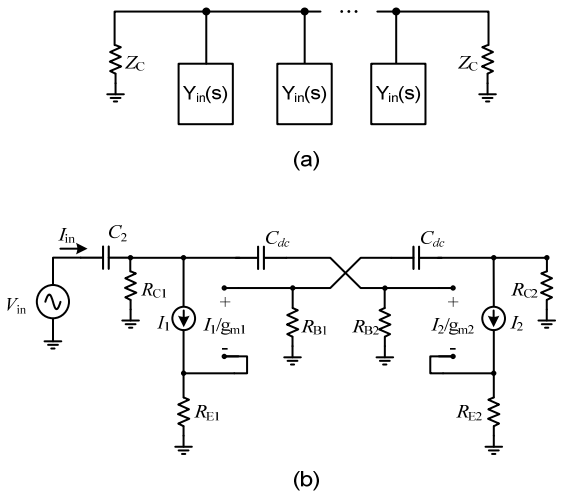

Fig. 3 Equivalent circuit used for the stability analysis in the low-frequency range. (a) Transmission line. (b) Circuit used to calculate Y_{in}, as the ratio between I_{in} and V_{in}.

Fig. 4 presents the evolution of the three roots of (8) versus the resistor R_{C1}. The results are compared with those obtained with pole-zero identification applied to two different circuits, simulated in microwave commercial software. One is the same equivalent circuit in Fig. 3 and the other is the realistic non-Foster transmission line, with full accurate models of all the active and passive elements, provided by Modelithics. As stated, the two have been simulated with microwave commercial software, applying pole-zero identification [31]-[33] to the impedance function $Z(f)$ extracted from this software. As shown in Fig. 4, the analytical results overlapped with the simulations of the simplified model and exhibit an excellent agreement with those corresponding to the accurately modeled circuit. In the latter case, to detect the negative real pole with very small magnitude, it has been necessary to consider a small frequency interval, going from zero to a few hundred Hertz. The advantage of the analytical formulation is the possibility of a direct evaluation of the Routh-Hurtwiz stability conditions at the design stage, since these conditions depend only on the coefficients of the characteristic polynomial. They can be easily checked after each variation of the biasing network elements and transistor-bias point.

An analytical formulation can also be derived for the case of bias networks based on inductive elements. This will give rise to a higher system order, as a result of the higher number of reactive elements. For simplicity, the circuit considered in the derivation has no resistors and DC feeds are used for a direct biasing of the transistor terminals. The resistor R_{E2} is eliminated, grounding the corresponding terminal, and the resistors R_{E1}, R_{B1}, R_{B2}, R_{C1} and R_{C2} are replaced with DC-feeds. In the most usual case of equal values for the DC-block capacitors and DC-feed inductors, given by L and C, the coefficients of the characteristic polynomial are:

$$\begin{aligned}
\alpha_7 &= (2G - 3g_{m2})\, g_{m1} C^3 L^4 \\
\alpha_6 &= (-GLg_{m1}g_{m2} + 12Cg_{m1} + 2CG)\, L^3 C^2 \\
\alpha_5 &= (7GLg_{m1} + 12C)\, C^2 L^2 \\
\alpha_4 &= (12g_{m1} + 7G)\, C^2 L^2 \\
\alpha_3 &= (5GLg_{m1} + 12C)\, CL \\
\alpha_2 &= (3g_{m1} + 5G)\, CL \\
\alpha_1 &= GLg_{m1} + 3C \\
\alpha_0 &= G
\end{aligned} \tag{10}$$

According to the Routh-Hurwitz criterion, if $3g_{m2} > 2G$ ($\alpha_7 < 0$), a sufficient condition for circuit instability is fulfilled. This is the case in the design considered here, having $g_{m2} = 32$ mS and $G = 20$ mS. Our results agree with previous observations [2], [9]-[10], stating that biasing networks based on inductors are more likely to give rise to instability.

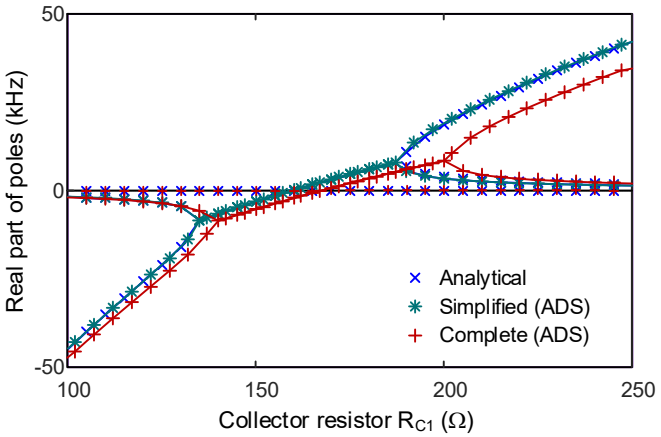

Fig. 4 Evolution of the three roots of (8) versus the resistor R_{C1}. The results are compared with those obtained with pole-zero identification applied to two different circuits, simulated in microwave commercial software. One is the same equivalent circuit in Fig. 3 and the other is the realistic non-Foster transmission line, with full accurate models of all the passive and active elements, provided by Modelithics.

As gathered from Fig. 4, the circuit becomes unstable from certain value of R_{C1}, in consistency with the reduction of the damping effect of this resistor, in parallel at the input port. The qualitative change of the stability is due to the crossing of a pair of complex-conjugate poles through the imaginary axis, which corresponds to a Hopf bifurcation [35]-[41]. Despite this, one should note that for most of the unstable interval, there are two real poles on the RHS, which should lead to a relaxation oscillation, in agreement with the results of the previous work [25]. In addition to the critical pair of complex conjugate poles, both the analytical formulation and pole-zero identification predict a negative real pole of very small magnitude. This will give rise to long transients, so the time-domain simulation of this kind of circuit should be extremely inefficient and/or inconclusive.

As gathered from our simplified system (8), instability cannot be due to the direct crossing through zero of a real pole. Mathematically, this would imply the fulfillment of equation (8) for $s = 0$ (real pole crossing the imaginary axis), leading to

the impossible condition $\alpha_0 = 0$ [see definitions in (9)]. The bifurcation can only be due to a pair of complex-conjugate poles crossing the imaginary axis. This is also seen in Fig. 2(c), even though the analysis in this figure corresponds to the full circuit, loaded with R and C_{neg}.

As shown in Fig. 4, after crossing the imaginary axis the pair of complex-conjugate poles splits into two real poles, which is indicative of a relaxation oscillation. These oscillations are associated with the periodical charging and discharging of circuit capacitors. They can be reasonably expected in a circuit based on resistive and capacitive elements. For validation the circuit has been experimentally characterized in the absence of the loading elements C_{neg} and R. Fig. 5 shows the measured spectra for different R_C values. The experimental results exhibit a very good agreement with the analytical and simulation predictions of Fig. 4. The dense spectral content observed in Fig. 5(c) and 5(d) is consistent with this kind of oscillation. There is an additional independent fundamental, which should have arisen from a secondary Hopf bifurcation of the oscillation predicted by the analysis in Fig. 4.

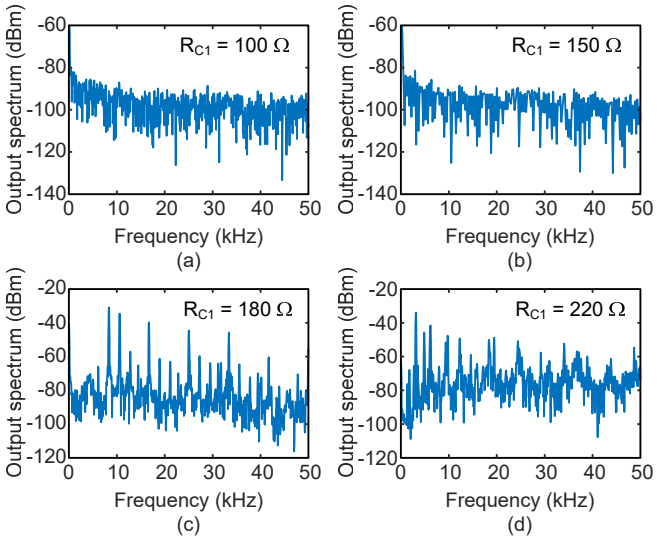

Fig. 5 Measured spectra for different R_C values. (a) $R_{C1} = 100\ \Omega$. Stable. (b) $R_{C1} = 150\ \Omega$. Stable. (c) $R_{C1} = 180\ \Omega$. Unstable. (d) $R_{C1} = 220\ \Omega$. Unstable.

The previous identification of the bifurcation phenomenon that gives rise to the low-frequency instability will allow a direct calculation of the stability boundary. Obtaining these boundaries is useful since they provide global information on the circuit stability properties and their evolution versus relevant circuit parameters. The qualitative stability change is due to a Hopf bifurcation [35]-[41], so the stability boundary in terms of any two convenient parameters can be calculated by replacing s with $j\omega$ in (8). Splitting the resulting complex equation into real and imaginary parts one obtains the following system of two real equations:

$$\begin{aligned} -\alpha_2\omega^2 + \alpha_0 = 0 \qquad (a) \\ -\alpha_3\omega^2 + \alpha_1 = 0 \qquad (b) \end{aligned} \tag{11}$$

Solving [11(b)] for ω^2 and replacing in [11(a)], the Hopf-bifurcation condition is derived:

$$\alpha_0\alpha_3 - \alpha_2\alpha_1 = 0 \tag{12}$$

Useful parameters to analyze the Hopf-bifurcation condition are R_{C1}, R_{C2}, g_{m1} and g_{m2}, since in the bipolar model the transconductance is approximate independent of the collector resistors. As an example, Fig. 6 presents the Hopf bifurcation locus in terms of R_{C1}, R_{C2}. As gathered from the figure, the circuit is stable for sufficiently small value of any these two resistors. The Hopf locus is in total agreement with the predictions of the stability analysis in Fig. 4, which was carried out for $R_{C2} = 75\ \Omega$. Measurements for different pairs of resistors have been carried out. Points with stable behavior are indicated with asterisks. Points with unstable behavior are indicated with squares. There is a very good agreement with the analytical predictions by (12).

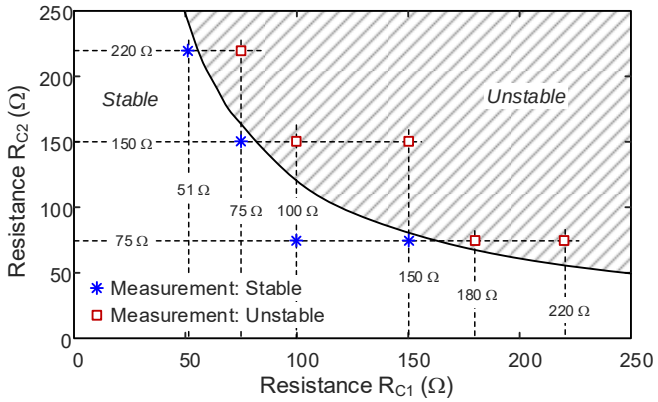

Fig. 6 Hopf-bifurcation locus in terms of the two resistors R_{C1}, R_{C2}, delimiting the region giving rise to instabilities detectable in the lower frequency interval. Measurements have been superimposed with good agreement.

IV. High-Frequency Instability

The high-frequency stability analysis will only be performed considering realistic models of all the active and passive elements in the non-Foster transmission line. This is due to the relevant impact of parasitic elements at high frequency. The stability analysis will be numerical and based on a combination of pole-zero identification and the Nyquist criterion. This should be able to predict both the low-frequency instabilities considered in Section III and the high frequency instabilities, associated with the impedance negation and other effects.

Two different components will be distinguished in the full circuit configuration: the passive transmission line, bounded by $Z_o = 50\ \Omega$ (or any other impedance values), and the N negative-impedance converters that periodically load this transmission line. Note that there can be changes affecting the passive line only, e. g., a variation in the number N of sections or an alteration of the termination impedances due to mismatch. For instance, instability arising when increasing N has been reported in [42], [44]. However, since the circuit operates in a linear regime, the input admittance $Y_{in}(s)$, exhibited by the NIC will remain the same, under this line modifications.

To derive the characteristic system resulting from a small perturbation at the frequency s, the schematic in Fig. 7 will be considered. The terminated passive line is described with an

$N\times N$ admittance matrix $\left[Y_L(s)\right]$, defined at the N ports where the N NICs are connected to this line. On the other hand, the N NICs are represented with an $N\times N$ diagonal matrix, with equal diagonal components given by the input admittance $Y_{in}(s)$, which is indicated as $diag\left[Y_{in}(s)\right]$. Then, the perturbed circuit must fulfill the following characteristic system:

$$\left\{\left[Y_L(s)\right]+diag\left[Y_{in}(s)\right]\right\}\Delta\bar{V}=0 \tag{13}$$

where $\Delta\bar{V}$ is the vector composed by the voltage increments at the NIC connection nodes, resulting from the small perturbation. Provided that there are no exact cancellations of RHS poles and zeroes in the function $Y_{in}(s)$ (which will be checked in a separate manner), the poles of the NIC-loaded transmission line will be given by the zeroes or roots of the following characteristic equation:

$$\det(s)=\det\left\{\left[Y_L(s)\right]+diag\left[Y_{in}(s)\right]\right\}=0 \tag{14}$$

As an example, in the case of the line with $N=3$ NIC elements, the above formulation particularizes to:

$$\det\left[Y(s)\right]= \det\left\{\begin{bmatrix} Y_{11}(s) & Y_{12}(s) & 0 \\ Y_{12}(s) & Y_{22}(s) & Y_{12}(s) \\ 0 & Y_{12}(s) & Y_{11}(s) \end{bmatrix}+\begin{bmatrix} Y_{in}(s) & 0 & 0 \\ 0 & Y_{in}(s) & 0 \\ 0 & 0 & Y_{in}(s) \end{bmatrix}\right\}=0 \tag{15}$$

As stated, due to the possible cancellation of RHS zeroes and poles in $Y_{in}(s)$, one must ensure that $Y_{in}(s)$ does not exhibit any RHS poles, as these would give rise to instabilities internal to the NIC that would not be detectable with (14).

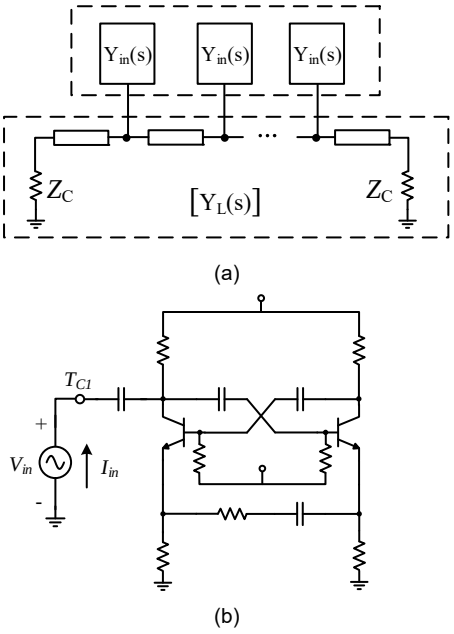

Fig. 7. Set-up for the numerical stability analysis of the non-Foster transmission line. (a) Linear matrix definition. (b) Numerical calculation of the input admittance of the individual NIC: $Y_{in}(j\omega)$. Pole-zero identification will be applied to this admittance-type transfer function.

In practice, the number of unstable circuit poles can be directly calculated in the microwave commercial software through an application of the Nyquist criterion [4], [22] to the determinant in (14). For this criterion to be usable, the function $\det(s)$ in (14) should not contain any RHS poles, since, as discussed in the introduction, $N_{cir}=N_Z-N_P$.

Because the matrix $\left[Y_L(s)\right]$ representing the terminated transmission line is passive, $N_P\neq 0$ may only come from possible RHS poles in the function $Y_{in}(s)$. Thus, $Y_{in}(s)$ should not exhibit any RHS poles, or, equivalently, as derived in the next paragraph, the NIC must be stable under a short circuit termination (SCS).

The NIC stability analysis under a short-circuit termination is carried out through pole-zero identification. To identify the function $Y_{in}(s)$, a series-voltage source is introduced [Fig. 7(b)] between the two nodes used for the NIC connection to the transmission line. Then, the ratio between the current circulating through this source and the voltage delivered provides a transfer function of admittance type. Absence of RHS poles in $Y_{in}(s)$ would indicate stability under a short circuit termination at the input port (SCS). As discussed, care must also be taken to check that there is no cancellation of RHS poles with RHS zeroes in the $Y_{in}(s)$ function, which is done by performing this identification at different locations of the NIC, under a short-circuit termination at the node where it is connected to the transmission line.

For $R_{C1}=150\ \Omega$ one obtains a stable NIC behavior under a short-circuit termination. The pole-zero locus obtained through the identification of $Y_{in}(s)$ is shown in Fig. 8(a). All the poles are on the left-hand side of the complex plane (LHS). To check for any possible RHS pole-zero cancellations, the identification has been applied to several transfer functions, defined at different NIC nodes. No RHS poles have been obtained in any case. The procedure has also also been applied under variations of the capacitance C_{neg} [Fig. 8(b)]. The poles remain on the LHS in all cases, so the Nyquist criterion should be applicable for any C_{neg}.

To obtain the Nyquist plot, the complex frequency s should be replaced by $j\omega$ in (14), which provides the function:

$$\det(j\omega)=\det\left\{\left[Y_L(j\omega)\right]+diag\left[Y_{in}(j\omega)\right]\right\} \tag{16}$$

Then, a sweep must be carried out in ω from zero to infinite, though in practice it is sufficient to sweep ω from zero to a maximum value, depending on the device gain and low-pass characteristic. Because the complex function considered [given by in (13)] contains no RHS poles, the number of unstable poles of the non-Foster transmission line will agree with number of clockwise encirclements of the Nyquist plot about the origin of the complex plane: $N_{cir}=N_Z$.

The described procedure has been initially applied in the case of $R_{C1}=150\ \Omega$ and $N=3$. In Fig. 9, the Nyquist plot has been traced for different values of C_{neg}, comprised between 5 pF and 16 pF. One can notice a high phase sensitivity about the point (0,0), which requires several zooms to evaluate the number of encirclements. As gathered from the expanded views of Fig. 9(b), the Nyquist plot does not encircle the origin for C_{neg} values below approximately 15.5 pF. However, it does encircle the origin for C_{neg} > 15.5 pF. This can be associated with the dominance of the negative capacitance in the non-Foster

transmission line from certain C_{neg}. The validity of the predictions obtained with the Nyquist plot have been checked with pole-zero identification applied to the entire non-Foster transmission line. In Fig. 10, the real part of the dominant pair of complex-conjugate poles has been represented versus C_{neg}. This pair of complex-conjugate poles crosses to the RHS at C_{neg} = 15.5 pF, in full agreement with the prediction of the Nyquist plot.

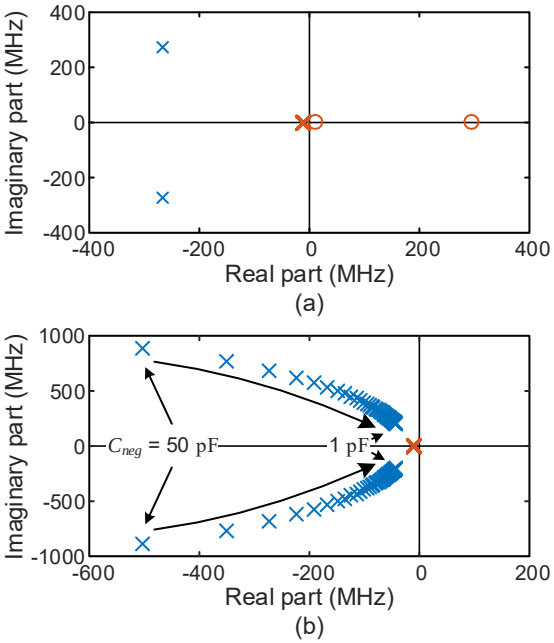

Fig. 8. Verification of the NIC stability prior to the stability analysis through the Nyquist plot. (a) Pole-zero locus obtained through the identification of $Y_{in}(s)$ for C_{neg} = 10 pF (b) Evolution of the real part of the dominant poles versus C_{neg}, indicating stable behavior for all the C_{neg} values.

The Nyquist criterion could not be used to detect the low-frequency instability, analyzed in Section III. This is because the standalone NIC is unstable under short-circuit terminations for some values of its resistive and capacitive components. Using the analysis in Section III, these components are selected in order to prevent the low frequency instability. Then, as verified in Fig. 8, the standalone NIC is stable under short-circuit terminations in the whole frequency range, so the Nyquist criterion can be applied to analyze the stability of the whole non-Foster transmission line.

The difficulties associated with the significant variations in the phase sensitivity of the Nyquist plot with respect to ω can be avoided by using a formulation of feedback type, based on the multiplication of the characteristic system (13) by the inverse of the passive matrix $[Y_L(s)]^{-1}$ (provided that the matrix is nonsingular). In the general case of $N\times N$ matrices, the resulting Nyquist determinant, of feedback type [32]-[33], is the following:

$$\det{}_{fb}(j\omega) = \det\left\{[U] + [Y_L(j\omega)]^{-1}\, diag[Y_{in}(j\omega)]\right\} = \det\left\{[U] + [Z_L(j\omega)]diag[Y_{in}(j\omega)]\right\} \quad (17)$$

where $[U]$ is the $N\times N$ diagonal matrix and $[Z_L(j\omega)]$ is the passive-impedance matrix, directly calculated with the commercial software. The feedback formulation involves a normalization effect, as the one demonstrated in [28]-[29]. The Nyquist plots obtained with the feedback formulation (17) for the same C_{neg} values are shown in Fig. 9(c) and Fig. 9(d). The same stability predictions are obtained, though the phase sensitivity is more even versus the perturbation frequency.

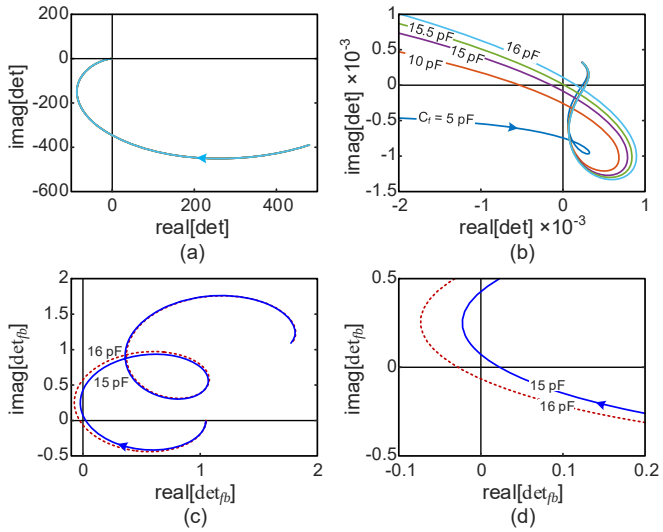

Fig. 9. Nyquist analysis in the case of a non-Foster transmission line with N = 3 elements and R_{C1} = 150 Ω. (a) Global view when using the function (16). (b) Expanded view when using the function (16). Unstable behavior is obtained for $C_{neg} \geq$ 15.5 pF. (c) Nyquist plots obtained when using the feedback formulation in (17) for the same set of C_{neg} values. (d) Expanded view.

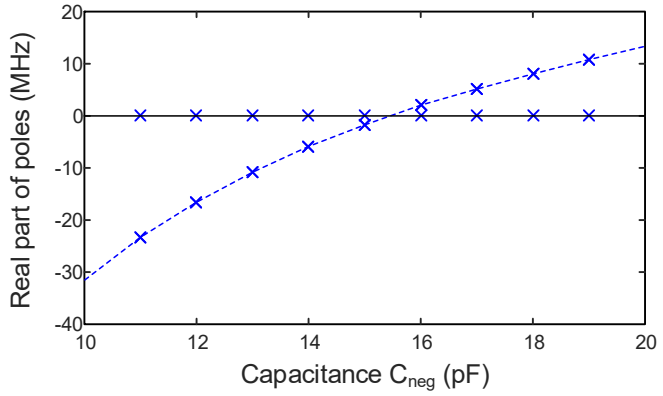

Fig. 10. Validation of the results of the Nyquist plots in Fig. 9 with pole-zero identification. The real part of the dominant pair of complex-conjugate poles has been represented versus C_{neg}. This pair of complex-conjugate poles cross to the RHS at C_{neg} = 15.5 pF, in full agreement with the prediction of the Nyquist plot.

Note that the Nyquist analysis and pole-zero identification are used here in a complementary manner. Pole-zero identification is applied only to the individual NIC to ensure the absence of RHS poles of $Y_{in}(s)$. This allows the application of the Nyquist criterion to the whole non-Foster transmission line, which can be done in the microwave commercial software through a simple computation of the matrices and determinant in (17), without any post-processing of the data. This enables a direct checking of the stability properties at the design stage. One advantage of the Nyquist criterion with respect to the pole-zero identification is the fact that the whole stability analysis is carried out through a single frequency sweep. It does not require splitting the perturbation frequency range (from dc to a very high value) into subintervals. We believe that this cooperative use of pole-zero identification and the Nyquist criterion can be of practical interest in other circuits with complex topologies.

As another example, the Nyquist criterion has been applied to a non-Foster transmission line containing $N = 10$ cells, using the feedback formulation (17). Under variations of C_{neg}, instability arises from much smaller value than in the case of only $N = 3$ cells. This is shown in Fig. 11, which compares the results obtained for $C_{neg} = 1$ pF and $C_{neg} = 3$ pF. For $C_{neg} = 1$ pF, the Nyquist plot does not encircle the origin, so the non-Foster transmission line is stable. For $C_{neg} = 3$ pF, the Nyquist plot encircles the origin twice, so the non-Foster transmission line should contain two pairs of unstable of poles on the RHS. This has been validated through the application of pole-zero identification to the whole transmission line. Results are shown in Fig. 12, where the real part of the dominant poles has been represented versus C_{neg}. In agreement with the predictions of the Nyquist plot, the circuit is stable at $C_{neg} = 1$ pF. In the neighborhood of $C_{neg} = 2.5$ pF, two pairs of complex-conjugate poles cross to the RHS, one after the other. For $C_{neg} = 3$ pF, the circuit is unstable with two pairs of complex-conjugate poles on the RHS, in agreement with the predictions of the Nyquist plot in Fig. 11.

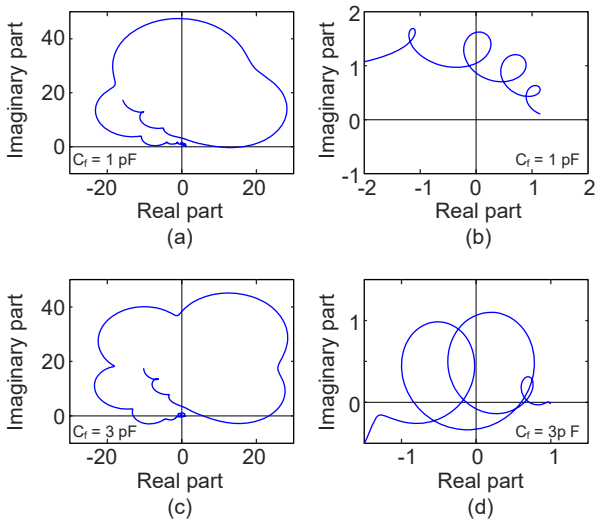

Fig. 11. Application of the Nyquist criterion to a non-Foster transmission line containing $N = 10$ cells, with $R_{C1} = 150\ \Omega$, using the feedback formulation (17) . (a) $C_{neg} = 1$ pF, global view of Nyquist plot, predicting stable beavior. (b) $C_{neg} = 1$ pF, expanded view. (c) $C_{neg} = 3$ pF, global view of Nyquist plot, predicting unstable behavior. (b) $C_{neg} = 3$ pF, expanded view.

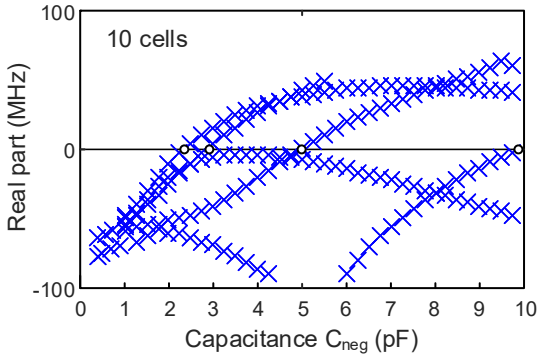

Fig. 12. Validation of the Nyquist plots through pole-zero identification applied to the entire non-Foster transmission line. The real part of the dominant poles has been represented versus C_{neg}. The circuit becomes unstable at about $C_{neg} = 2.5$ pF. Two pairs of complex-conjugate poles cross to the RHS one after the other.

V. Hopf-Bifurcation Locus

As has been shown in the various stability analyses versus relevant circuit parameters, the qualitative change of stability is due to the crossing of a pair of complex-conjugate poles through the imaginary axis, which corresponds to a Hopf bifurcation [37]-[40],[45]. This is, in fact, the most usual instability mechanism in a circuit operating in small signal, since a real pole crossing through zero would imply either a turning point or a branching point in the DC solution curve [35]-[37], which are relatively rare.

On the other hand, the observation of several consecutive crossing of complex-conjugate poles through the imaginary axis is indicative of the possible existence of several Hopf locus sections or even disconnected loci. Here a methodology for the direct tracing of Hopf bifurcation locus, with no need for continuation methods, is proposed. This is based on a matrix formulation, with a judicious choice of the reference ports, as many as the number N of NICs. In fact, the N ports will be defined between nodes loaded with equivalent passive branches, containing elements that do not affect the transistor biasing, since those elements will be considered as unknowns of the bifurcation equation. The non-Foster transmission line will be opened at ports defined between the nodes where the capacitance C_{neg}, in series with the resistor R, is connected to the structure (Fig. 13). As will be shown, this facilitates the calculation of the instability boundaries, even in the case in which the resistor R is absent, which would simply correspond to the particular situation $R = 0\ \Omega$. The NxN impedance matrix defined as indicated in Fig. 13 will be denoted $\left[Z_{cir}(\eta, s)\right]$. Note that this matrix contains both passive and active elements.

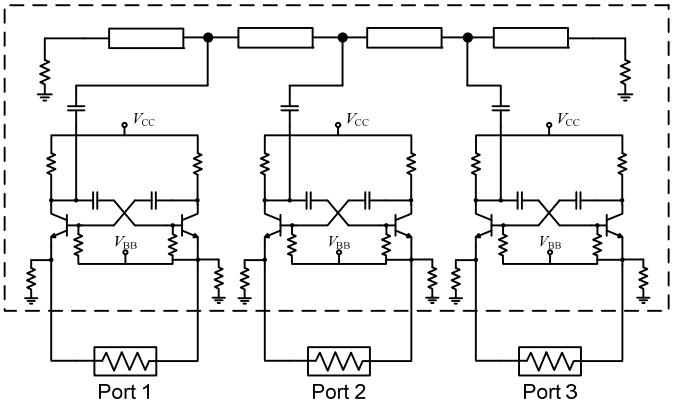

Fig. 13. Calculation of the impedance/admittance matrices with ports defined between the nodes where the elements R and C_{neg} should be connected to the whole configuration.

The stability boundary defined by the Hopf-bifurcation locus is calculated in terms C_{neg} and R, plus an additional parameter η. This parameter will correspond to any quantity with a relevant impact on the stability properties, such as a bias voltage. For the calculation of the Hopf locus, the frequency s in the characteristic determinant should be replaced with $j\omega$. In terms of $[Z_{cir}(\eta, j\omega)]$, the Hopf bifurcation condition is given by:

$$\det(j\omega, R, C_{neg}, \eta) = \det\left\{[Z_{cir}(\eta, j\omega)] + diag\left[R + \frac{1}{C_{neg}\, j\omega}\right]\right\} = 0 \quad (18)$$

where the second impedance matrix is diagonal, with equal diagonal elements, given by the impedance of the series connection of R and C_{neg}. For illustration, the formulation will be particularized to the case $N = 3$, which provides:

$$\det(j\omega, R, C_{neg}, \eta) = \det\left\{\begin{bmatrix} Z_{11}(\eta, j\omega) & Z_{12}(\eta, j\omega) & Z_{13}(\eta, j\omega) \\ Z_{12}(\eta, j\omega) & Z_{22}(\eta, j\omega) & Z_{12}(\eta, j\omega) \\ Z_{13}(\eta, j\omega) & Z_{12}(\eta, j\omega) & Z_{11}(\eta, j\omega) \end{bmatrix} + \begin{bmatrix} R + \frac{1}{C_{neg}\, j\omega} & 0 & 0 \\ 0 & R + \frac{1}{C_{neg}\, j\omega} & 0 \\ 0 & 0 & R + \frac{1}{C_{neg}\, j\omega} \end{bmatrix}\right\} = 0 \quad (19)$$

For each value of the parameter η, the complex equation (18) provides a system of two real equations in the three unknowns ω, R, C_{neg}, which will give rise to a curve or locus in the plane defined by R and C_{neg}. In practice, the locus is calculated in a simple manner by sweeping ω from zero to a maximum value, and solving the two real equations obtained for each ω in terms of R and C_{neg}. Note that splitting (18) into real and imaginary parts provides two coupled polynomial equations in R and C_{neg}. The system is solved by exporting the matrix $[Z_{cir}(\eta, j\omega)]$ from the commercial microwave software and using a program such a Matlab to compute the roots in R and C_{neg} for each ω value. Under a sufficiently fine sweep in η, it is also possible to obtain the Hopf-bifurcation locus (or loci) in the plane η and C_{neg} for a constant R value ($R = 0$, for instance).

The analysis described has been applied to the non-Foster transmission line in Fig. 1, containing $N = 3$ NICs. The extra parameter η is the base-bias voltage V_{BB}. Solving (19), one obtains the ensemble of Hopf bifurcation loci in Fig. 14(a), in the plane defined by R and C_{neg}. As can be seen there are two distinct Hopf loci for each V_{BB}, which is consistent with the observation of two pairs of complex-conjugate poles in Fig. 2(b) and Fig. 11. The loci in solid line correspond to $V_{BB} = 0.8$ V. The loci in dashed line correspond to $V_{BB} = 0.85$ V and the loci in dotted line correspond to $V_{BB} = 0.95$ V. The unstable regions are shadowed, using a different color for each V_{BB}.

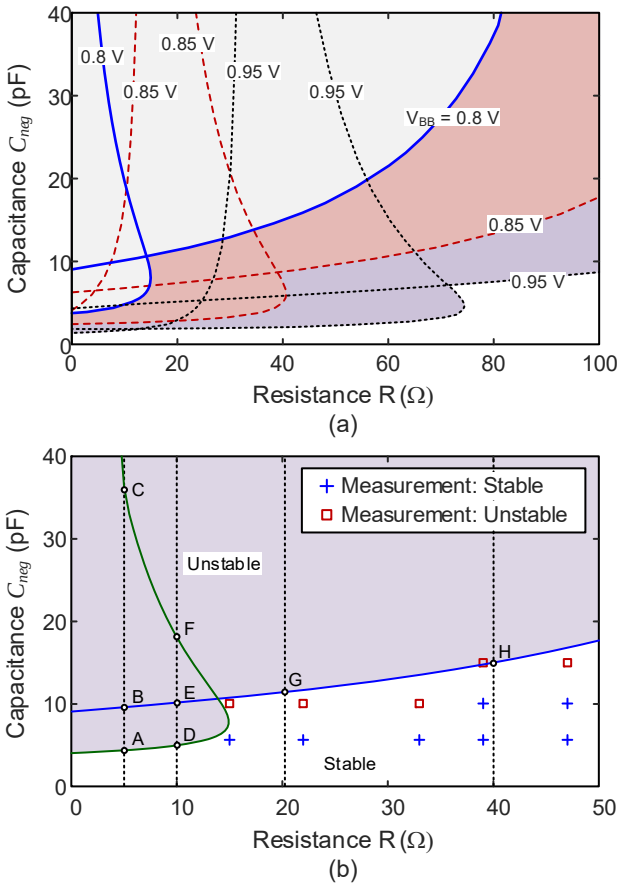

Fig. 14. Ensemble of Hopf-bifurcation loci in the plane defined by R and C_{neg}. (a) Results obtained by solving (19), with the additional parameter $\eta = V_{BB}$. The loci in solid line correspond to $V_{BB} = 0.8$ V. The loci in dashed line correspond to $V_{BB} = 0.85$ V and the loci in dotted line correspond to $V_{BB} = 0.95$ V. The unstable regions are shadowed, using a different color for each V_{BB}. (b) Hopf bifurcation loci obtained for $V_{BB} = 0.8$ V. The points A, B, to H in Fig. 14(b) indicate the Hopf bifurcation points validated through pole-zero identification in Fig. 15. Measurements for different pairs (C_{neg}, R) are superimposed. Capacitors used belong to the ATC Ceramics 600S series (Design Kits 26T and 27T).

Note that obtaining the Hopf bifurcation loci through continuation plus parameter switching [38] would have been

cumbersome, due to the presence of turning points and the mentioned existence of two disconnected loci. In fact, when using continuation to trace the loci, and due to its local quality, one of the two disconnected loci could have been missed.

Fig. 14(b) shows in more detail the two Hopf bifurcation loci obtained for V_{BB} = 0.8 V, which has been thoroughly validated through pole-zero identification. At each R value, the circuit is stable for C_{neg} values below the Hopf loci, which corresponds to a smaller impact of the negated impedance on the non-Foster transmission line. Note that this negated impedance is introduced in parallel at the NIC locations, so a smaller effect is obtained for smaller C_{neg} and larger R, proving impedances with larger magnitude, connected in parallel. The predictions of the two disconnected loci in Fig. 14(b) have been validated through a detailed pole-zero identification of the whole structure. The points A, B, to H in Fig. 14(b) indicate the Hopf bifurcation points validated through pole-zero identification in Fig. 15, where they are denoted in the same manner. In a first attempt, the bifurcation corresponding to the upper locus was not detected when performing the identification at the base terminal of the left NIC transistor in Fig. 7(b). It was necessary to change the observation node to T_{C1} [see Fig. 7(b)], the one corresponding to the connection between the NIC and the transmission line.

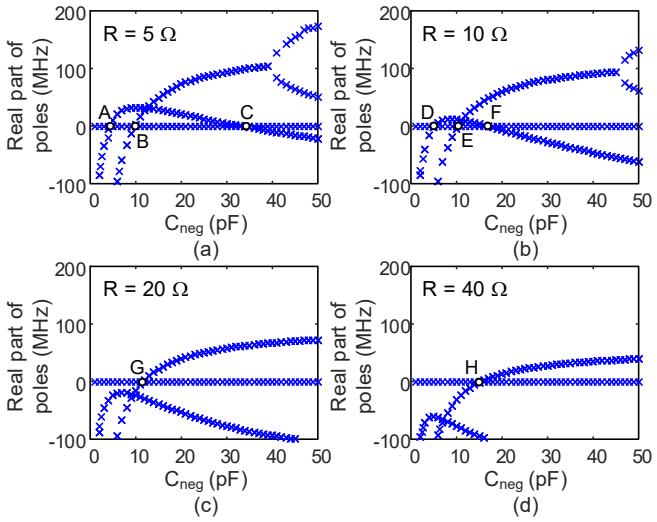

Fig. 15. Variation of the real part of the dominant poles represented versus C_{neg} for different values of R. The four vertical paths followed in the identification are indicated in Fig. 14(b). (a) R = 5 Ω. (a) R = 10 Ω. (c) R = 20 Ω. (d) R = 40 Ω.

Fig. 15 shows the variation of the real part of the poles versus C_{neg} for different values of R. The four vertical paths followed in the identification of Fig. 15 are indicated in Fig. 14(b). As can be seen, there is an excellent agreement between the predictions of the loci in Fig. 14(b) and the results of the pole-zero identification in Fig. 14. In consistency with Fig. 12, for the lower R values there are two distinct pairs of complex-conjugate poles crossing to the RHS.

The stability boundary in Fig. 14 has been validated experimentally. Fig. 14(b) shows the results corresponding to V_{BB} = 0.8 V. Squares indicate unstable points, whereas crosses correspond to stable points. Note that standard discrete capacitor (ATC Ceramics 600 series) and resistor values were used for these measurements. Taking into account the effect of V_{BB}, additional validations have been performed. A pair of values of R and C_{neg} in the stable zone is selected and the bias voltage is increased until the circuit becomes unstable, in agreement with Fig. 14(a). At the stability change, the pair of values should belong to the Hopf locus for the particular V_{BB}. The procedure has been repeated for different pairs of R and C_{neg}. Fig. 16 shows the results of this procedure for two pairs of element values (R = 39 Ω, C_{neg} = 10 pF) and (R = 22 Ω, C_{neg} = 5.6 pF). As seen in Fig. 14(a), at V_{BB} = 0.8 V the circuit should be stable for the two pairs of values. The corresponding spectra are shown in Fig. 16(a) and Fig. 16(c). In each case, when increasing V_{BB} from 0.8V the loci will cross the pair of values C_{neg} and R giving rise to the onset of an oscillation at V_{BB} = 0.82 V [Fig. 16(b)] and V_{BB} = 0.85 V [Fig. 16(d)], respectively.

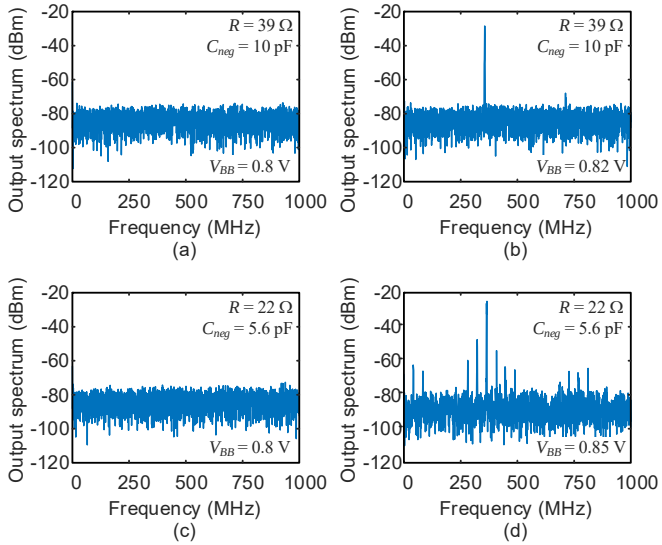

Fig. 16. Experimental validation of the Hopf loci shown in Fig. 14.(a) and (b) Spectra for R = 39Ω, C_{neg} = 10 pF and V_{BB} = 0.8V (stable) and V_{BB} = 0.82 V (unstable), respectively. (c) and (d) Spectra for R = 22 Ω, C_{neg} = 5.6 pF and V_{BB} = 0.8 V (stable) and V_{BB} = 0.85V (unstable), respectively.

Note that the Hopf loci in Fig. 14(a) enable a straightforward determination of the stability properties and stability margin for R = 0 Ω, which is just a particular point of the horizontal axis. The Hopf loci for R = 0 Ω in the plane defined by V_{BB} and C_{neg} are calculated as follows. The bias voltage V_{BB} is swept (the step used is 50 mV), solving the complex equation (19) at each sweep step, in terms of R and C_{neg}. This gives the ensemble of solution points, in terms of V_{BB}, C_{neg} and R, that fulfill Re(det) = 0 and Im(det) = 0. Interpolation of these data for R = 0 provides two different contours:

$$\begin{aligned} &\mathrm{Re}\left[\det\left(V_{BB},C_{neg}\right)/R=0\ \Omega\right]=0 \quad (a)\\ &\mathrm{Im}\left[\det\left(V_{BB},C_{neg}\right)/R=0\ \Omega\right]=0 \quad (b) \end{aligned} \tag{20}$$

Then, the Hopf locus or loci (since there can be more than one) are given by the intersection points of the two contours. Following the procedure described, it has been possible to

directly obtain the three Hopf loci in Fig. 17(a), which have been validated with pole-zero identification and experimental measurements (superimposed). Fig. 17(b)-(d) present the results of pole-zero identification for three different values of the bias voltage V_{BB} (0.76 V, 0.8 V and 0.82 V). In each case, there is full agreement between the predictions by the loci in Fig. 17(a) and the crossings of the various pairs of complex-conjugate poles through the imaginary axis. Regarding the measurement results superimposed in Fig. 17(a), there is also a very good agreement. Only the first Hopf bifurcation, that is, the one that occurs from a stable DC solution can be measured, since the other ones, occurring from an unstable DC solution are unphysical.

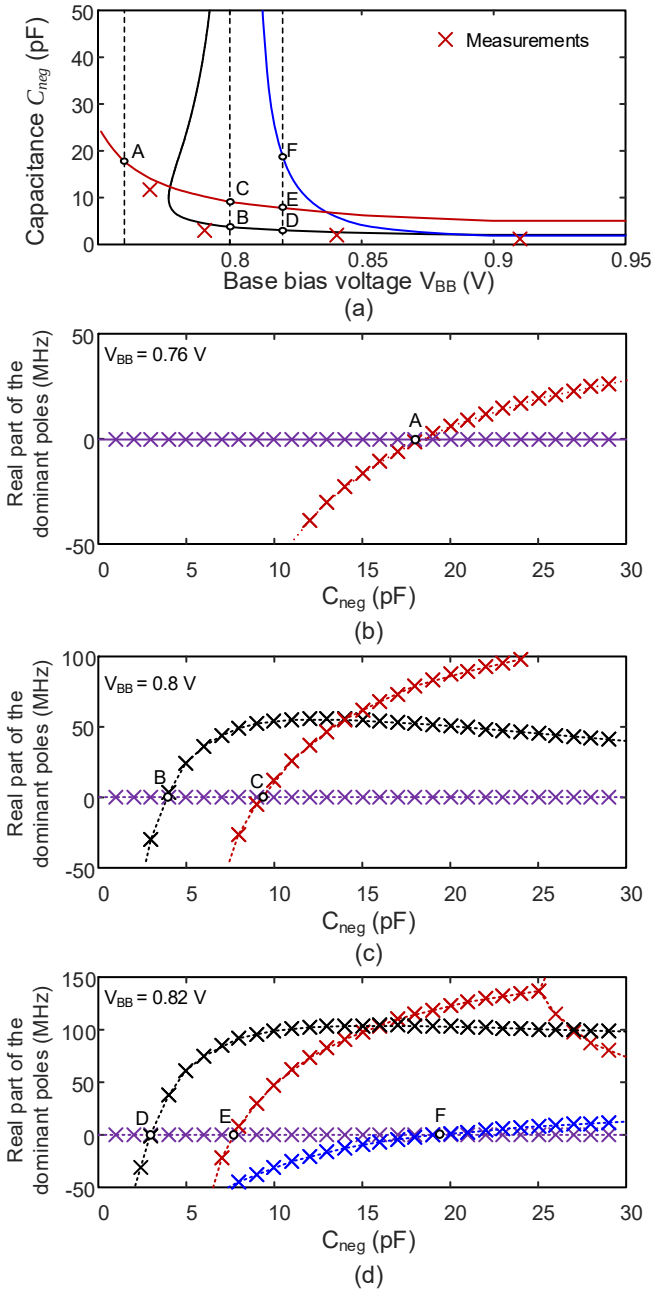

Fig. 17 Hopf loci of the non-Foster transmission line for $R = 0\ \Omega$. (a) Loci in the plane defined by the bias voltage V_{BB} and C_{neg}. Measurement points at the instability boundaries are superimposed. (b) Validation through pole-zero identification for $V_{BB} = 0.76$ V. (c) $V_{BB} = 0.8$ V. (c) $V_{BB} = 0.82$ V.

We would like to emphasize that with the new method, the Hopf loci are calculated in an efficient manner, which demands neither optimization nor continuation techniques. It requires just a frequency sweep in commercial microwave software, together with the resolution of the two real equations obtained by splitting (18) into real and imaginary parts in a mathematical program. The loci will enable an insightful understanding of the evolution of the circuit stability properties.

As a final comment, one can gather some information on the tolerance effects from inspection of the bifurcation loci in Fig. 6, corresponding to the low-frequency instability, and in Fig. 14, corresponding to the high frequency instability (although this assumes equal values of R and C_{neg}). To ensure robustness against tolerances, one should choose an operation point far from the Hopf bifurcation loci that constitute the stability boundaries. Additional loci can be traced in terms of other parameters with a likely impact on the stability properties. A more detailed way to predict the impact of tolerances is to perform pole-zero identifications combined with a Monte-Carlo analysis, as presented in [46].

VI. Conclusion

A series of methodologies for the in-depth stability analysis and stabilization of non-Foster circuits containing multiple NIC elements have been presented. An analytical formulation has been derived to predict instabilities detectable in the lower frequency range, which can be avoided through a direct evaluation of the Routh-Hurwitz criterion at the design stage. The instability boundaries in terms of two significant parameters are calculated through a computation of the Hopf locus, derived from the analytical expressions. Instabilities detectable at higher frequencies are predicted with a numerical method that combines the pole-zero identification of the individual NIC element with the Nyquist criterion applied to a feedback formulation of the non-Foster transmission line. The stability boundaries are obtained through the root calculation of a determinant function, obtained from an N-port impedance matrix, easily extracted from commercial microwave software. This enables a direct computation of all the coexisting bifurcation loci, with no need for continuation techniques. All the results of the new methodologies have been rigorously validated with pole-zero identification and with measurements.

References

[1] S. E. Sussman-Fort, R. M. Rudish, "Non-Foster Impedance Matching of Electrically-Small Antennas," *IEEE Trans. Antennas Propag.*, vol. 57, no. 8, pp. 2230-2241, Aug. 2009.

[2] C. R. White, J. S. Colburn, R. G. Nagele, "A Non-Foster VHF Monopole Antenna," *IEEE Antennas Wireless Propag. Lett.*, vol. 11, pp. 584-587, 2012.

[3] C. K. Kuo, "Realization of negative-immittance converters and negative resistances with controlled sources," PhD dissertation, School of Electrical and Computer Engineering, Georgia Institute of Technology, Atlanta, GA, 1967

[4] H. Mirzaei, G. V. Eleftheriades, "A Resonant Printed Monopole Antenna with an Embedded Non-Foster Matching Network," *IEEE Trans. Antennas Propag.*, vol. 61, no. 11, pp. 5363-5371, Nov. 2013.

[5] A. M. Elfrgani, R. G. Rojas, “Successful realization of Non-Foster circuits for wide-band antenna applications,” 2015 IEEE MTT-S Int. Microw. Symp., Phoenix, AZ, pp. 1-4, 2015.

[6] H. Mirzaei, G. V. Eleftheriades, “Unilateral non-Foster elements using loss-compensated negative-group-delay networks for guided-wave applications,” 2013 IEEE MTT-S International Microwave Symposium Digest, Seattle, WA, pp. 1-4, 2013.

[7] J. G. Linvill, “Transistor Negative Impedance Converters,” Proc. IRE, vol. 41, pp. 725-729, June 1953.

[8] J. G. Linvill, and R. L. Wallace, “Negative Impedance Converters Employing Transistors,” U.S. Patent, 2726370, Dec. 6, 1955.

[9] R. Nealy, “Investigation of a Negative Impedance Converter for Wide Band Antenna Matching,” Bradley Dept. of Electrical & Computer Engineering, Virginia Tech, Blacksburg, VA, Project Report No. 28, Sept., 2012.

[10] K.S. Song, “Non-Foster Impedance Matching and Loading Networks for Electrically Small Antennas,” Ph.D. dissertation, Ohio State University, Columbus, OH, 2011.

[11] J. Long, M. Jacob, D. Sievenpiper, “Broadband Fast-Wave Propagation in a Non-Foster Circuit Loaded Waveguide,” IEEE Trans. Microw. Theory Techn., vol. 62, no. 4, pp. 789-798, Apr. 2014.

[12] J. Long, D. Sievenpiper, "Stable Multiple Non-Foster Circuits Loaded Waveguide for Broadband Non-Dispersive Fast-Wave Propagation", Electronics Letters, vol. 50, no. 23, pp. 1708-1710, 2014.

[13] H. Mirzaei, G. V. Eleftheriades, “Arbitrary-angle squint-free beamforing in series-fed antenna arrays using non-Foster elements synthesized by negative-group-delay networks,” *IEEE Trans. Antennas Propag.*, vol. 63, no. 5, pp. 1997-2010, May, 2015.

[14] H. Mirzaei, G. V. Eleftheriades, “Squint-free beamforing in series-fed antenna arrays using synthesized non-Foster elements,” 2013 IEEE Antennas and Propagation Society International Symposium (APSURSI), Orlando,FL, pp. 2209-2210, 2013.

[15] H. Mirzaei, G. V. Eleftheriades, “An active artificial transmission line of squint-free series-fed antenna array applications,” 41st European Microwave Conference, Manchester, UK, pp. 503-506, 2011.

[16] M.C. Tang, N. Zhu, R. Ziolkowski. “Augmenting a modified Egyptian axe dipole antenna with non-Foster elements to enlarge its directivity bandwidth,” IEEE Antennas and Wireless Propagation Letters, vol. 12, pp. 421-424, 2013.

[17] E. Ugarte-Muñoz, S. Hrabar, D. Segovia-Vargas, and A. Kiricenko, “Stability of non-Foster reactive elements for use in active metamaterials and antennas,” IEEE Trans. Antennas Propag., vol. 60, no. 7,pp. 490–3494, Jul. 2012.

[18] S. Hrabar, I. Krois, A. Kiricenko, I. Bonic, Ivan. (2010). Homogenization of active transmission-line-based ENZ metamaterials. 1 - 4. 10.1109/APS.2010.5562256.

[19] M. Barbuto, A. Monti, F. Bilotti, A. Toscano, “Design of a non-Foster actively loaded SRR and application in metamaterial-inspired components,” IEEE Transactions on Antennas and Propagation, vol. 61, pp.1219-1227, 2013.

[20] Z. Ning, R. Ziolkowski, “Active metamaterial-inspired broad-bandwidth, efficient, electrically small antennas,” IEEE Antennas Wireless Propag. Lett., vol. 10, no. 1, pp. 1582–1585, Jan. 2011.

[21] S. D. Stearns, “Circuit stability theory for non-Foster circuits,” *2013 IEEE MTT-S Int. Microw. Symp.*, Seattle, WA, pp. 1-3, 2013.

[22] A. M. Elfrgani, R. G. Rojas, “Stabilizing non-Foster circuits for electrically small antennas,” 2014 IEEE Antennas and Propagation Society International Symposium (APSURSI), Memphis, TN, pp. 464-465, 2014.

[23] M. Jacob, D. Sievenpiper, “Gain and Noise Analysis of Non-Foster Matched Antennas,” IEEE Trans. Antennas Propag., vol. 64, no. 12, pp. 4993-5004, Dec., 2016.

[24] J. Brownlie, “On the Stability Properties of a Negative Impedance Converter,” IEEE Trans. Circuit Theory, vol. 13, no. 1, pp. 98-99, Mar., 1966.

[25] A. Suárez, F. Ramírez, “Circuit-level stability and bifurcation analysis of non-Foster circuits,” 2017 IEEE MTT-S Int. Microwave Symp., Honolulu, HI, USA, June, 2017.

[26] K. Ogata, Modern Control Engineering, Prentice Hall PTR, Upper Saddle River, NJ, 2001

[27] V. Rizzoli and A. Lipparini, “General stability analysis of periodic steady-state regimes in nonlinear microwave circuits,” *IEEE Trans. Microw. Theory Techn.*, vol. 33, no. 1, pp. 30–37, Jan., 1985.

[28] A. Platzker and W. Struble, “Rigorous determination of the stability of linear n-node circuits from network determinants and the appropriate role of the stability factor K of their reduced two-ports,” in Proc. 3rd Int. Workshop Integrated Nonlinear Microwave Millimeterwave Circuits, Oct. 5–7, 1994, pp. 93–107.

[29] W. Struble and A. Platzker, “A rigorous yet simple method for determining stability of linear N-port networks [and MMIC application],” in Proc. 15th Gallium Arsenide Integrated Circuit Symp., 1993, pp. 251–254.

[30] R. W. Jackson, "Rollett proviso in the stability of linear microwave circuits-a tutorial," in *IEEE Transactions on Microwave Theory and Techniques*, vol. 54, no. 3, pp. 993-1000, March 2006.

[31] J. Jugo, J. Portilla, A. Anakabe, A. Suárez, J. M. Collantes, “Closed-loop stability analysis of microwave amplifiers,” IEE Electronics Letters, vol. 37, pp. 226-228, Feb., 2001.

[32] A. Anakabe, J.M. Collantes, J. Portilla, J. Jugo, A. Mallet, L. Lapierre, J.P. Fraysse, “Analysis and Elimination of Parametric Oscillations in Monolithic Power Amplifiers”, 2002 IEEE MTT-S International Microwave Symposium Digest, Seattle, WA, pp. 2181-2184, 2002.

[33] N. Ayllon, J. M. Collantes, A. Anakabe, I. Lizarraga, G. Soubercaze-Pun, S. Forestier, “Systematic approach to the stabilization of multitransistor circuits,” IEEE Trans. Microwave Theory & Tech., vol. 59, no. 8, pp 2073-2082, Aug. 2011.

[34] C. R. White, J. W. May, and J. S. Colburn, “A variable negative-inductance integrated circuit at UHF frequencies,” IEEE Microw. Wireless Compon. Lett., vol. 22, no. 1, pp. 35–37, Jan. 2012.

[35] S. Wiggins, Introduction to Applied Nonlinear Dynamical Systems and Chaos, Springer-Verlag, New York, 1990.

[36] J. Guckenheimer and P. Holmes, Nonlinear Oscillations, Dynamical Systems and Bifurcations of Vector Fields, Springer-Verlag, New York, 1990.

[37] J. M. T. Thompson and H. B. Stewart. Nonlinear dynamics and chaos. John Wiley & Sons,Ltd., second edition, 2002.

[38] A. Suárez, Analysis and Design of Autonomous Microwave Circuits. IEEE-Wiley, Hoboken, (NJ) Jan. 2009.

[39] R. Quere, E. Ngoya, M. Camiade, A. Suarez, M. Hessane, and J. Obregon, "Large signal design of broadband monolithic microwave frequency dividers and phase-locked oscillators," IEEE Trans. Microw. Theory Techn., vol. 41, no. 11, pp. 1928-1938, Nov. 1993.

[40] A. Suárez, R. Quéré, Stability Analysis of Nonlinear Microwave Circuits, Artech-House Publishers, Boston, 2003.

[41] V. Rizzoli and A. Neri, "State of the art and present trends in nonlinear microwave CAD techniques," IEEE Trans. Microwave Theory Tech., vol. 36, no. 2, pp. 343–356, Feb., 1988.

[42] S. Rengarajan, C. R. White, “Stability analysis of superluminal waveguides periodically loaded with non-Foster circuits,” *IEEE Antennas Wireless Propag. Lett*., vol. 12, pp. 1303-1306, 2013.

[43] C. C. Hu, Modern Semiconductor Devices for Integrated Circuits, Upper Saddle River, N.J: Prentice Hall, 2010.

[44] J. Long, “Non-Foster Circuit Loaded Periodic Structures for Broadband Fast and Slow Wave Propagation,” PhD dissertation, School of Electrical and Computer Engineering, University of California San Diego, La Jolla, CA, 2015.

[45] A. Suárez, S. Jeon, D. Rutledge, "Stability analysis and stabilization of power amplifiers," IEEE Microwave Magazine, vol. 7, pp. 51-65, Oct., 2006.

[46] J. M. Collantes, N. Otegi, A. Anakabe, N. Ayllón, A. Mallet and G. Soubercaze-Pun, "Monte-Carlo stability analysis of microwave amplifiers," *WAMICON 2011 Conference Proceedings*, Clearwater Beach, FL, 2011, pp. 1-6.

Almudena Suárez (M'96–SM'01–F'12) was born in Santander, Spain. She received the Electronic Physics and Ph.D. degrees from the University of Cantabria, Santander, Spain, in 1987 and 1992, respectively, and the Ph.D. degree in Electronics from the University of Limoges, Limoges, France, in 1993.

She is currently a Full Professor with the Communications Engineering Department, University of Cantabria. She co-authored *Stability Analysis of Nonlinear Microwave Circuits* (Artech House, 2003) and authored *Analysis and Design of Autonomous Microwave Circuits* (IEEE-Wiley, 2009).

Prof. Suárez is a member of the Technical Committees of the IEEE Microwave Theory and Techniques Society (IEEE MTT-S) International Microwave Symposium (IMS) and the European Microwave Conference. She was an IEEE Distinguished Microwave Lecturer from 2006 to 2008. She is a member of the Board of Directors of the *European Microwave Association*. She was the Coordinator of the Communications and Electronic Technology Area for the Spanish National Evaluation and Foresight Agency between 2009 and 2013. In 2014 and 2015 she was the co-chair of IEEE Topical Conference on RF Power Amplifiers (PAWR). Prof. Suárez is the Editor-in-Chief of the *International Journal of Microwave and Wireless Technologies* from Cambridge University Press journals and an Associate Editor for *IEEE Microwave Magazine*.

Franco Ramírez was born in Potosí, Bolivia. He obtained a degree in electronic systems engineering degree from the Military School of Engineering (EMI) in La Paz, Bolivia, in 2000 and the Ph.D. degree in communications engineering from the University of Cantabria, Santander, Spain in 2005. From 1999 to 2000, he worked for Ericsson de Bolivia Telecomunicaciones, where he was involved in several projects related with GSM and TDMA technologies. From 2009 to 2005, Dr. Ramírez was a Research Fellow of the "Ramón y Cajal" Programme, funded by the Spanish Ministry of Science and Innovation, at the Communications Engineering Department of the University of Cantabria, where he is currently an Associate Professor. His research interests include phase noise, stability and the development of nonlinear techniques for the analysis and design of autonomous microwave circuits.